Permeability Macromodels for Magnetic Powder Materials Under DC Bias

Permeability Macromodels for Magnetic Powder Materials under DC Bias

Arne Schröder, *Member, IEEE*, Tommaso Bradde, *Member, IEEE*, Dierk Bormann, Alexandru Savca, and Stefano Grivet-Talocia, *Fellow, IEEE*

***Abstract*—Magnetic powder materials are often considered for inductors used in high-current applications due to their high saturation flux densities and good high-frequency performance. For the design and optimization of powder-based high-frequency inductors, it is important to consider permeability spectra with superimposed DC bias. To include those properties in system-level circuit simulations, compact macromodels are required. Therefore, this work proposes a black-box model and a phenomenological model, providing equivalent circuits for the permeability of magnetic material under DC bias. The accuracy of both models is investigated using measured permeability spectra of commercial powder core materials. Application examples are outlined to illustrate the benefits of those macromodels. It is demonstrated that the black-box model provides very accurate results over the entire range of parameters for all materials, while the phenomenological model in its present, simple form and gives satisfactory results only for selected magnetic materials, in the frequency range of interest.**

I. Introduction

OPTIMIZING magnetic components is crucial for obtaining maximum efficiency and minimum volume and cost of power electronic converters and systems. Depending on the magnetic component and its application, various types of magnetic materials, such as ferrites, powder cores, or nanocrystalline alloys, are used [1]. In the field of electromagentic compatibility (EMC), common mode chokes carrying relatively low net currents often consist of low-loss ferrites or nanocrystalline cores [2]. When applied for high current application, air gaps need to be introduced for those materials. Introducing air gaps comes with a number of disadvantages, such as stray fields and resulting air gap losses [3]. Therefore, magnetic powder cores are often considered [1], [4], [5]. Powder cores exhibit very good saturation properties, low losses, and low hysteresis [6]. For electromagnetic noise reduction, powder cores are applied in differential mode (DM) filters, see for instance [7], [8].

EMC system-level analyses and design of power converters are often carried out in time domain using circuit simulations. For this, equivalent circuits representing the high-frequency properties of the main converter components, including the magnetics, are required. Cauer-type models in conjunction with hysteresis and saturation models for ferrites and nanocrystalline materials have been proposed in [9]. This model was later extended to capture dimensional resonance effects [10]. Higher-order Debye models with several discrete relaxation times were used in [11], and a general Debye relaxation process was applied by [12] to describe the complex permeability of magnetic powder cores.

In many applications, magnetic cores used in EMC filters experience a certain low-frequency (50 Hz or 60 Hz) or DC net current, which partially saturates the magnetic material and alters its high-frequency (HF) permeability spectrum. This is especially true for DM filters or single turn bus-bar dampers [13]. EMC filters and associated HF inductors are often designed using simulation-based multi-objective optimization [8], [14]. In this context, the HF performance is one main optimization criteria besides loss, volume, cost, etc. The HF performance of inductors is determined by various effects, such as stray capacitances to ground, turn-to-turn capacitances of coils, the magnetic material used and its permeability spectrum under DC bias. Compact models covering all those mechanisms are required for optimal design of EMC filters. Accordingly, an adequate description for the HF permeability as a function of the biasing current represents a relevant asset to guide the design and the analysis of magnetic components. The HF properties of magnetic materials are typically characterized by measuring their permeability spectra under different DC bias conditions, e.g., following the workflow outlined in [15]. In order to exploit the information provided by these measurements in system-level circuit simulations, bias-dependent equivalent circuits matching the measured responses are necessary. Modeling losses of magnetic materials under DC bias has been adressed by [16], [17] and recently, many works adressed data-driven magnetic material modeling and design using machine learning and artificial inteligence [18], [19] with focus on B-H loop and loss calculations. However, only few works target the macromodeling of magnetic permeability spectra under DC bias. In [20], Foster-type networks derived from measurements have been employed to describe the complex impedance of DC-biased nanocrystalline cores. To identify the network elements, the authors of [21] used a machine learning approach. A phenomenological model was proposed in [15], capturing permeability spectra over a wide range of frequencies and bias currents with only three fitting parameters. This model results in Foster-like networks with bias dependent elements. The main disadvantage of these approaches is that they are restricted to permeability spectra which exhibit a (higher order) relaxational Debye behavior. This is often not sufficient for describing permeability spectra, for example if the measured cores exhibit dimensional resonances [22].

To overcome the shortcomings affecting the above state-of-the-art methods, we propose the application of behavioral parameterized macromodeling algorithms in this work. Such approaches are black-box, meaning that they do not introduce physical assumptions to guide the modeling procedure. In

this setting, the only objective is to provide the user with a compact model (macromodel) that reproduces the response of the underlying component in a system-level simulation [23], performed either in time or frequency domain. Starting from a set of measurements characterizing the behavior of interest, the ultimate goal of these techniques is to generate an equivalent circuit that, for all admissible bias conditions

1) reproduces the behavior of the core/coil over a prescribed bandwidth,
2) is of manageable complexity, and
3) preserves the passivity of the underlying component.

All the above requirements are equally important. A model not fulfilling 1 or 2 would imply misleading or inefficient simulations, respectively. A model lacking passivity may be the root cause of spurious numerical instabilities when used in a system level simulation [24]. In the last decades, a large number of publications have addressed this subject, see e.g. [25]–[28].

The remainder of this paper is organized as follows. Section II introduces the magnetic powder materials under consideration and briefly describes their experimental characterization. Section III outlines two different types of macromodels for modeling permeability spectra. Sec. IV benchmarks the macromodels, using permeability spectra of example materials, and Sec. V illustrates the application of the macromodels in converter-level analysis and design. Finally, conclusions are drawn in Sec. VI.

In this article, vectors are denoted with bold lowercase letters (e.g. $\mathbf{x}$), matrices with uppercase bold letters (e.g. $\mathbf{X}$). The symbol $\mathrm{j} = \sqrt{-1}$ is the imaginary unit, while $s = \alpha + \mathrm{j}\omega$ is the Laplace variable. With $\mathcal{S}^n$, we denote the set of symmetric matrices of size n. The expression $\mathbf{A} \succ \mathbf{B}$ means that the matrix $\mathbf{A} - \mathbf{B}$ is positive definite. Similarly, $\mathbf{A} \succeq \mathbf{B}$ means that the matrix $\mathbf{A} - \mathbf{B}$ is positive semidefinite.

II. Experimental Characterization

This section introduces the magnetic powder materials considered and their experimental permeability characterization. The complex permeability under DC bias can be expressed as

$$\mu_\mathrm{r}(\mathrm{j}\omega, I_\mathrm{DC}) = \mu_\mathrm{r}'(\mathrm{j}\omega, I_\mathrm{DC}) - \mathrm{j}\,\mu_\mathrm{r}''(\mathrm{j}\omega, I_\mathrm{DC})\,. \tag{1}$$

Here, I_DC denotes the superimposed bias current and ω denotes the angular frequency. In this work, four different powder materials are investigated. Figure 1 illustrates the magnetic cores used in experiments and Tab. I summarizes their main properties. These materials were chosen for their different characteristics in terms of cost, bias properties, losses, and frequency properties, and also because they are frequently used in industrial converters.

The complex permeability spectra were determined by impedance measurements of magnetic cores using the setup proposed in [15]. This setup is based on shorted coaxial cavities which contain the magnetic cores under investigation. In contrast to other commonly used setups which involve multiple turns around cores, the considered setup can be used up to several hundreds of MHz, as it does not suffer from coil self-resonances. Permeability spectra were determined

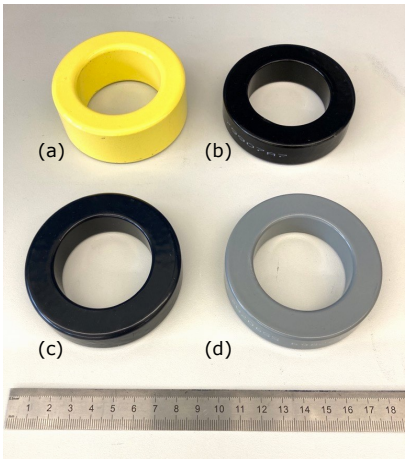

Fig. 1. Cores under consideration: (a) *Mix -26*, (b) *Mega Flux*, (c) *Kool Mμ MAX*, (d) *MPP*.

TABLE I
Main properties of considered magnetic powder cores investigated in this work. l_E denotes the magnetic path length, A_E is the effective cross section, A_L denotes the (unbiased) inductance, and B_SAT is the saturation flux density.

Material	***Mix 26***	***Mega Flux***	***Kool Mμ MAX***	***MPP***
Alloy	Fe	Fe-Si	Fe-Si-Al	Fe-Ni-Mo
Core ID	T300-26	CK77860	0079907A7	55907A2
Manufact.	Micrometals	CSC	Magnetics	Magnetics
Initial μ_r	75	60	60	60
l_e	198 mm	200 mm	196 mm	196 mm
A_e	338 mm^2	277 mm^2	221 mm^2	221 mm^2
A_L	160 nH	85 nH	85 nH	85 nH
B_sat	1.38 T	1.6 T	1.0 T	0.8 T

between 10 kHz and 110 MHz, for bias currents between 0 kA and 2.5 kA, which corresponds to bias H fields between 0 Oe and 160 Oe for the considered core geometries. For more details, we refer the reader to [15].

For each of the considered cores, the experiments return a set of measurements of the permeability spectra (1), sampled at discrete frequency-bias configurations. Introducing two indices $k = 1, \ldots, K$ and $m = 1, \ldots, M$, these measurements are denoted as

$$\mu_\mathrm{r}^{k,m} = \mu_\mathrm{r}(\mathrm{j}\omega^k, I_\mathrm{DC}^m) \in \mathbb{C}, \tag{2}$$

with $\omega^k \in 2\pi[0.01, 110]$ MHz, $I_\mathrm{DC}^m \in [0, 2.5]$ kA $\equiv \mathcal{I}$. Using (2), the impedance of an inductor consisting of P stacked cores and N turns can be expressed as

$$Z^{k,m} = Z(\mathrm{j}\omega^k, I_\mathrm{DC}^m) = \mathrm{j}\omega^k \mu_\mathrm{r}^{k,m} \mu_0 \beta \in \mathbb{C}\,, \tag{3}$$

where

$$\beta = PN^2 \frac{A_e}{l_e} \tag{4}$$

denotes the geometry factor in which A_e is the effective cross section of a magnetic core and l_e denotes its magnetic path length. Please note that (3) does not account for stray inductances nor stray turn-to-turn capacitances of windings. These effects need to be considered separately.

III. Macromodeling

Equivalent circuits for powder cores are required when performing EMC analysis and design based on circuit simulations. This section describes two different approaches for equivalent circuit synthesis.

A. Black-Box Macromodeling Approach

The black-box modeling approach applied in this work is adapted from [29], where a general algorithm is described for generating guaranteed passive parameterized macromodels, starting from the set of measurements (3). The main idea of the method is to represent the macromodel in terms of its parameterized small-signal impedance $\hat{Z}(s, I_{\text{DC}}) \in \mathbb{C}$, and to require it to match the coil impedance $Z(s, I_{\text{DC}})$, whenever $I_{\text{DC}} \in \mathcal{I}$. This is done exploiting the available measurements to enforce the approximation condition

$$\hat{Z}(\mathrm{j}\omega^k, I_{\text{DC}}^m) \approx Z^{k,m}, \quad k = 1, \dots, K \quad m = 1, \dots, M, \quad (5)$$

with high accuracy. Concurrently, the method guarantees that the two following important features are retained $\forall I_{\text{DC}} \in \mathcal{I}$:

1) $\hat{Z}(s, I_{\text{DC}})$ is a reduced-order rational function of the variable s, and
2) $\hat{Z}(s, I_{\text{DC}})$ represents the impedance function of a passive network, meaning that it is a Positive Real (PR) function, fulfilling the following requirements [30]

$$\hat{Z}(s, I_{\text{DC}}) \text{ is regular for } \mathrm{Re}(s) \geq 0 \quad \forall I_{\text{DC}} \in \mathcal{I}, \quad (6)$$

$$\hat{Z}^*(s, I_{\text{DC}}) = \hat{Z}(s^*, I_{\text{DC}}) \quad \forall s \in \mathbb{C}, \forall I_{\text{DC}} \in \mathcal{I}, \quad (7)$$

$$\hat{Z}(\mathrm{j}\omega, I_{\text{DC}}) + \hat{Z}^*(\mathrm{j}\omega, I_{\text{DC}}) \geq 0 \quad \forall \omega \in \mathbb{R}, \forall I_{\text{DC}} \in \mathcal{I}. \quad (8)$$

The above features allow to easily cast the macromodel in the form of a linear passive equivalent circuit, (e.g., following the procedure introduced in [31]), that can be seamlessly used to represent the coil behavior in any system-level-simulation. The modeling workflow is briefly recalled in the following.

1) Model Structure: The employed approach is enabled by the definition of the following barycentric form

$$\hat{Z}(s, I_{\text{DC}}) = \frac{\mathsf{N}(s, I_{\text{DC}})}{\mathsf{D}(s, I_{\text{DC}})} = \frac{\sum_{i=0}^{n} r_i(I_{\text{DC}})\varphi_i(s)}{\sum_{i=0}^{n} p_i(I_{\text{DC}})\varphi_i(s)}, \quad (9)$$

where $\varphi_0(s) = 1$ and $\varphi_i(s) = (s - q_i)^{-1}$ for $i = 1, \dots, n$ are partial fractions with $\mathrm{Re}(q_i) < 0$. This set of "basis functions" induce a rational dependence on s of $\hat{Z}(s, I_{\text{DC}})$. The dependence on I_{DC} is induced by the parameterized numerator and denominator coefficients

$$r_i(I_{\text{DC}}) = \sum_{\ell=0}^{\bar{\ell}} r_{i,\ell}\, \xi_\ell(I_{\text{DC}}), \quad p_i(I_{\text{DC}}) = \sum_{\ell=0}^{\bar{\ell}} p_{i,\ell}\, \xi_\ell(I_{\text{DC}}), \quad (10)$$

where $\xi_\ell(I_{\text{DC}})$ define a set of parameter-dependent basis functions of cardinality $\bar{\ell}$ while $r_{i,\ell}, p_{i,\ell} \in \mathbb{C}$ are unknown constants that need to be determined through a fitting procedure. Both q_i and the associated $r_{i,\ell}$, $p_{i,\ell}$ are either real or appear in complex conjugate pairs to guarantee the physical realizability of the model (9). Noticing that both $\mathsf{N}(s, I_{\text{DC}})$, $\mathsf{D}(s, I_{\text{DC}}) \in \mathbb{C}$ are rational functions sharing the same set of poles $\{q_i\}$, one can easily check that these poles cancel out in (9). As a consequence, the numerator and denominator of $\hat{Z}(s, I_{\text{DC}})$ are the numerator polynomials of $\mathsf{N}(s, I_{\text{DC}})$ and $\mathsf{D}(s, I_{\text{DC}})$.

Straightforward computations show that the coefficients of such polynomials are linear combinations of $r_i(I_{\text{DC}})$ and $p_i(I_{\text{DC}})$ respectively. Hence, both the zeros and the poles of $\hat{Z}(s, I_{\text{DC}})$ are parameterized by I_{DC}. The latter coincide with the zeros of $\mathsf{D}(s, I_{\text{DC}})$. This fact is illustrated by the following simple example.

Example III.1. Let $n = 2$. The model structure (9) reads:

$$\hat{Z}(s, I_{\text{DC}}) = \frac{r_0(I_{\text{DC}}) + \frac{r_1(I_{\text{DC}})}{s - q_1} + \frac{r_2(I_{\text{DC}})}{s - q_2}}{p_0(I_{\text{DC}}) + \frac{p_1(I_{\text{DC}})}{s - q_1} + \frac{p_2(I_{\text{DC}})}{s - q_2}} \quad (11)$$

$$= \frac{a_2(I_{\text{DC}})s^2 + a_1(I_{\text{DC}})s + a_0(I_{\text{DC}})}{b_2(I_{\text{DC}})s^2 + b_1(I_{\text{DC}})s + b_0(I_{\text{DC}})} \quad (12)$$

with

$$\begin{aligned}
&a_2(I_{\text{DC}}) = r_0(I_{\text{DC}}),\ b_2(I_{\text{DC}}) = p_0(I_{\text{DC}}),\\
&a_1(I_{\text{DC}}) = -r_0(I_{\text{DC}})(q_1 + q_2) + r_1(I_{\text{DC}}) + r_2(I_{\text{DC}}),\\
&b_1(I_{\text{DC}}) = -p_0(I_{\text{DC}})(q_1 + q_2) + p_1(I_{\text{DC}}) + p_2(I_{\text{DC}}),\\
&a_0(I_{\text{DC}}) = r_0(I_{\text{DC}})q_1q_2 - r_2(I_{\text{DC}})q_1 - r_1(I_{\text{DC}})q_2,\\
&b_0(I_{\text{DC}}) = p_0(I_{\text{DC}})q_1q_2 - p_2(I_{\text{DC}})q_1 - p_1(I_{\text{DC}})q_2.
\end{aligned}$$

State-of-the-art approaches based on the model structure (9) build parameterized behavioral models based on different choices of the basis functions $\xi_\ell(I_{\text{DC}})$, ranging from rational functions [32] to radial basis functions [28] and orthogonal polynomials [31]. The choice of the polynomial basis is proven to be flexible and effective in many applications including those regarding the parameterization of small-signal transfer functions with respect to a set of biasing DC quantities, see e.g. [26], [33], [34]. In this work we set

$$\xi_\ell(I_{\text{DC}}) = b_\ell^{\bar{\ell}}(I_{\text{DC}}) \quad (13)$$

where $b_\ell^{\bar{\ell}}(I_{\text{DC}})$ is the ℓ-th Bernstein polynomial of degree $\bar{\ell}$. As shown in [29], this choice enables the formulation of a deterministic black-box modeling workflow that guarantees the stability and the passivity of the resulting equivalent circuit throughout the space of admissible bias conditions $\mathcal{I}$, as outlined in the following sections.

2) Fitting strategy: Based on model structure (9), the fitting condition (5) is enforced in least-squares sense, applying the so-called Parameterized Sanathanan-Koerner (PSK) iteration [32], [35]. Since a direct enforcement of (5) would require solving a nonlinear least-squares problem in the variables $p_{i,\ell}$, the employed method iteratively solves a sequence of linearized and re-weighted linear least-squares problems. At iteration μ, the algorithm enforces the approximation condition

$$\frac{\mathsf{N}^\nu(\mathrm{j}\omega^k, I_{\text{DC}}^m) - \mathsf{D}^\nu(\mathrm{j}\omega^k, I_{\text{DC}}^m)Z^{k,m}}{\mathsf{D}^{\nu-1}(\mathrm{j}\omega^k, I_{\text{DC}}^m)} \approx 0, \quad \forall k, \forall m \quad (14)$$

where superscript ν denotes the model evaluated using the estimates of the coefficients available at iteration ν. Assuming the initialization $\mathsf{D}^0(\mathrm{j}\omega, I_{\text{DC}}) = 1$, the condition (14) that is solved at iteration ν is linear in the unknowns $r_{i,\ell}^\nu, p_{i,\ell}^\nu$, since

the quantity $\mathsf{D}^{\nu-1}$ is known as a result of the previous iteration. The iteration stops when

$$\mathsf{D}^{\nu}(\mathrm{j}\omega, I_{\text{DC}}) \simeq \mathsf{D}^{\nu-1}(\mathrm{j}\omega, I_{\text{DC}}), \tag{15}$$

that is, when the denominator estimate reaches a fixed point. When this condition is met (14) becomes equivalent to (5). Stacking the variables $p^{\nu}_{i,\ell}$ in the vector $\mathbf{p}^{\nu} = (p^{\nu}_{0,0}, p^{\nu}_{0,1}, \ldots, p^{\nu}_{n,\bar{\ell}})^T$, a possible numerical check for convergence is

$$C^{\nu} = \frac{\left\|\mathbf{p}^{\nu} - \mathbf{p}^{\nu-1}\right\|_2}{\left\|\mathbf{p}^{\nu-1}\right\|_2} \leq \epsilon, \tag{16}$$

where ϵ is a positive user defined tolerance. Alternatively, the algorithm can be stopped when stagnation of model against data error is observed, or when a maximum number of iterations is reached. We remark that the PSK algorithm can be interpreted as a generalization of the well-known Vector Fitting (VF) iteration [36] for performing rational fitting of multivariate functions.

In order to enforce (14), one needs only the availability of the denominator variables $\mathbf{p}^{\nu}$ computed at the previous iteration. Building on this fact, the method introduced in [37] shows how to perform the PSK iteration by eliminating the numerator coefficients $r^{\nu}_{i,\ell}$. It can be easily shown (see [37]) that (14) reduces to the following algebraic minimum-norm condition

$$\min_{\mathbf{p}^{\nu}} \left\|\mathbf{\Gamma}^{\nu}\mathbf{p}^{\nu}\right\|_2, \tag{17}$$

where $\mathbf{\Gamma}^{\nu}$ is a known regression matrix. The trivial all-zero solution is ruled out using the standard approach introduce in [38]. Assuming that the convergence condition (16) is met at iteration $\bar{\nu}$, the model generation is completed by estimating the remaining numerator variables $r_{i,\ell}$. Collecting such variables in the vector $\mathbf{r} = (r_{0,0}, r_{0,1}, \ldots, r_{n,\bar{\ell}})^T$, model completion is performed by solving the problem

$$\min_{\mathbf{r}} \left\|\mathbf{\Phi}\mathbf{r} + \mathbf{\Gamma}^{\bar{\nu}}\mathbf{p}^{\bar{\nu}}\right\|_2 \tag{18}$$

where $\mathbf{\Phi}$ is again a known data matrix.

3) Passivity constraints: The fitting strategy recalled in the previous section is aimed at enforcing the accuracy requirement (5). However, in its plain formulation, it does not guarantee that the resulting model impedance $\hat{Z}(s, I_{\text{DC}})$ fulfils all of the required passivity conditions (6), (7), (8). In particular, while (7) is inherently guaranteed upon including complex conjugate pole/residue pairs in the model structure (9) (a standard practice in rational approximation and VF algorithms), suitable numerical constraints must be enforced when solving problems (17) and (18) in order to guarantee that (6) and (8) hold.

In particular, condition (6) requires that for each admissible configuration of the bias current, $\hat{Z}(s, I_{\text{DC}})$ has only poles with strictly negative real part, so that the corresponding equivalent circuit is asymptotically stable. As observed in [31], a sufficient condition entailing the stability of model (9) at each PSK iteration is the following parameterized frequency-domain inequality (see [29, Sec. IV] for further details)

$$\mathsf{D}^{\nu}(\mathrm{j}\omega, I_{\text{DC}}) + \mathsf{D}^{\nu *}(\mathrm{j}\omega, I_{\text{DC}}) > 0 \quad \forall \omega \in \mathbb{R}, \forall I_{\text{DC}} \in \mathcal{I}. \tag{19}$$

Incorporating constraint (19) into the optimization problem (17) would guarantee that the resulting denominator estimate generates a stable model. Condition (19) represents a convex yet infinite dimensional constraint on the optimization variables $\mathbf{p}^{\nu}$ and is thus numerically intractable. It is shown in [29] that under model structure (9) defined upon the choice (13), the constraint (19) admits a relaxed representation in terms of a set of linear matrix inequalities of the form

$$\mathbf{L}_c(\mathbf{p}^{\nu}, \mathbf{P}_c) \succ 0, \quad c = 1, \ldots, \bar{\ell}, \tag{20}$$

where $\mathbf{P}_c \in \mathcal{S}^n$ are additional instrumental unknowns and the matrix functions $\mathbf{L}_c(\mathbf{p}^{\nu}, \mathbf{P}_c) : (\mathbb{R}^{(n+1)(\bar{\ell}+1)} \times \mathcal{S}^n) \to \mathcal{S}^{n+1}$ are affine in $\mathbf{p}^{\nu}, \mathbf{P}_c$. This last fact makes (20) convex [39], and efficiently tractable via off-the-shelf solvers that can handle semi-definite programming. We refer the reader to [29] for proofs and derivations; here we highlight that enforcing (20) while solving (17) guarantees the fulfilment of (19), hence model stability as a byproduct.

The macromodel passivity enforcement strategy is completed by guaranteeing the last missing property (8). This is done by constraining the optimization problem (18), after the convergence of the PSK iteration is attained. With $D^{\bar{\nu}}(s, I_{\text{DC}})$ fixed and known, (8) represents again a convex infinite dimensional constraint on the optimization variables $\mathbf{r}$ of (18). Also in this case, it can be proved that under the working assumptions (8) is implied by a set of Linear Matrix Inequalities (LMIs) of the form

$$\mathbf{S}_j(\mathbf{r}, \mathbf{V}_j) \succeq 0, \quad j = 1, \ldots, 2\bar{\ell}, \tag{21}$$

with $\mathbf{V}_j \in \mathcal{S}^n$ are additional instrumental unknowns and $\mathbf{S}_j(\mathbf{r}, \mathbf{V}_j) : (\mathbb{R}^{(n+1)(\bar{\ell}+1)} \times \mathcal{S}^n) \to \mathcal{S}^{n+1}$ are again affine in $\mathbf{r}, \mathbf{V}_j$. See [29, Sec. V] and [40, Sec 4.4]. Once problem (18) is solved under constraints (21), the model is completed and $\hat{Z}(s, I_{\text{DC}})$ fulfills properties (6), (7), (8), so that passivity is guaranteed by construction.

4) Equivalent Circuit Synthesis: Applying the procedure outlined in the previous sections returns a macromodel $\hat{Z}(s, I_{\text{DC}})$ under the barycentric transfer function representation (9). For the sake of system level simulation, this macromodel can be cast into a SPICE compatible, fully behavioral, equivalent circuit, as outlined in [31]. The proposed synthesis approach maintains the smooth parameterization of the equivalent circuit coefficients with the aim of avoiding numerical issues in SPICE transient simulations. We report here the synthesis approach for macromodels in admittance representation, from which the impedance case can be inferred by duality.

Let $Y(s) = \mathsf{N}(s, I_{\text{DC}})\,\mathsf{D}(s, I_{\text{DC}})^{-1}$ with $\mathsf{N}(s, I_{\text{DC}})$ and $\mathsf{D}(s, I_{\text{DC}})$ structured as in (9). The synthesis is based on interconnecting individual equivalent circuits for the involved instrumental quantities, as follows. The functions $\mathsf{D}(s, I_{\text{DC}})$, $\mathsf{N}(s, I_{\text{DC}})$ are synthesized as one-port admittances $Y_D(s, I_{\text{DC}})$ and $Y_N(s, I_{\text{DC}})$ respectively. Defining with $V_D(s)$, $I_D(s)$ the electrical variables related to $Y_D(s, I_{\text{DC}})$ and with $V_N(s)$,

$I_N(s)$ those related to $Y_N(s, I_{\rm DC})$, we have the relations

$$I_D(s) = Y_D(s, I_{\rm DC})V_D(s), \quad V_D(s) = Y_D^{-1}(s, I_{\rm DC})I_D(s)$$
$$I_N(s) = Y_N(s, I_{\rm DC})V_N(s), \quad V_N(s) = Y_N^{-1}(s, I_{\rm DC})I_N(s). \tag{22}$$

These two networks are depicted in the top and middle schematics of Fig. 2. The model in admittance representation $Y(s, I_{\rm DC})$ relates the input voltage $V(s)$ to the output current $I(s)$ as

$$I(s) = Y(s, I_{\rm DC}) = \mathsf{N}(s, I_{\rm DC}) \cdot \mathsf{D}^{-1}(s, I_{\rm DC})V(s). \tag{23}$$

This relation is recovered by enforcing

$$I(s) = I_N(s), \quad I_D(s) = V(s), \quad V_N(s) = V_D(s), \tag{24}$$

via the controlled sources of Fig. 2. Exploiting (24) and (22) allows to write

$$I(s) = Y_N(s, I_{\rm DC})V_D(s) = Y_N(s, I_{\rm DC}) \cdot Y_D^{-1}(s, I_{\rm DC})I_D(s) =$$
$$= Y_N(s, I_{\rm DC}) \cdot Y_D^{-1}(s, I_{\rm DC})V(s) = \mathsf{N}(s, I_{\rm DC}) \cdot \mathsf{D}^{-1}(s, I_{\rm DC})V(s), \tag{25}$$

which shows that $Y(s, I_{\rm DC})$ is the admittance seen looking into the terminals of the interface circuit depicted at the bottom of Fig. 2. Thus, the problem of the equivalent circuit synthesis is reduced to that of synthesizing the admittances $Y_N(s, I_{\rm DC})$ and $Y_D(s, I_{\rm DC})$.

An equivalent circuit for $Y_D(s, I_{\rm DC})$ is obtained by decomposing the current $I_D(s)$ as

$$I_D(s) = \mathsf{D}(s, I_{\rm DC})\, V_D(s) = \sum_{i=0}^{n} I_{D,i}(s) \tag{26}$$

where $I_{D,0}(s) = p_0(I_{\rm DC})\, V_D(s)$, and

$$I_{D,i}(s) = p_i(I_{\rm DC})\, V_{C,i}(s), \quad \text{with} \quad V_{C,i}(s) = \frac{V_D(s)}{(s - q_i)}, \tag{27}$$

for $i = 1, \ldots, n$. With real stable basis poles $q_i < 0$, the instrumental voltage $V_{C,i}(s)$ is synthesized through a standard RC cell, see Fig. 3 (top). Two coupled RC cells are used realize a pair of complex conjugate basis poles $q_{i+1} = q_i^*$, see [23]. The instrumental currents $I_{D,i}(s)$ are synthesized as voltage-controlled current sources with parameterized transconductance $p_i(I_{\rm DC})$. Equation (26) is then realized as in Fig. 3 (bottom). The synthesis of $Y_N(s, I_{\rm DC})$ follows the same lines.

For further illustration of the approach, the interested reader can find one equivalent circuit netlist as a free access item in the additional material to this article.

B. Phenomenological Model

Next, a previously published phenomenological model is summarized. For details, we refer the reader to [15]. A simple, phenomenological description of the frequency- and bias-dependent permeability is a Debye-type relaxational model, based on the idea that the response of each magnetic grain is characterized by a single relaxation rate ω_0, expected to be roughly equal to the frequency at which the magnetic skin depth in the grain material is of the order of the grain size. A closer analysis leads to the approximate relation

$$\omega_0 \approx \frac{4\pi^2}{\mu_{\rm ri}\mu_0\sigma_{\rm i}a_0^2}\,, \tag{28}$$

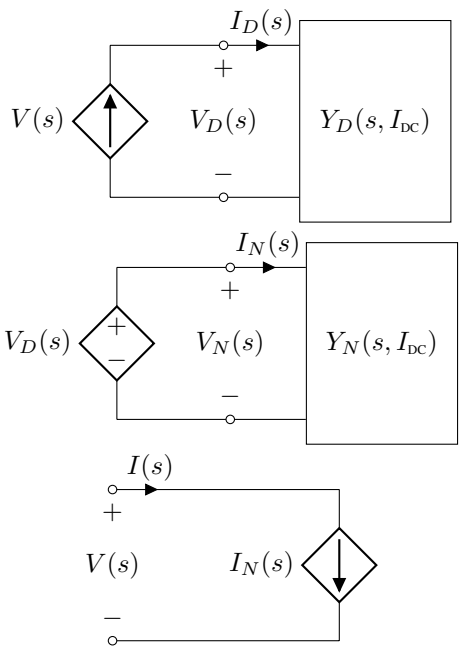

Fig. 2. Behavioral SPICE netlist synthesis for black box macromodels in admittance representation. Top: denominator sub-block. Middle: numerator sub-block. Bottom: external interface of the behavioral model.

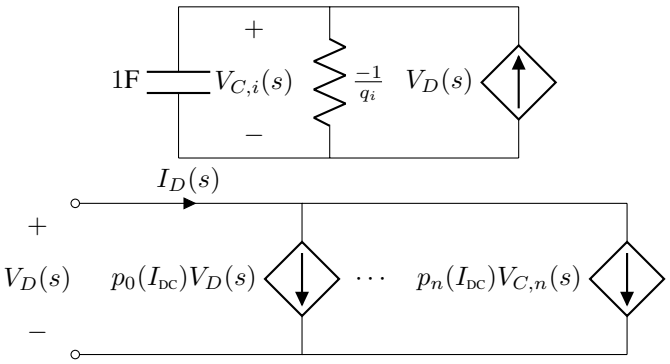

Fig. 3. Synthesis $\mathsf{D}(s, I_{\rm DC})$ in admittance representation. Top: elementary RC cell synthesizing the basis pole q_i. Bottom: external circuit interface.

where $\mu_{\rm ri}$ and $\sigma_{\rm i}$ denote the intrinsic relative permeability and electrical conductivity, respectively, of the grain material, and a_0 is some typical grain diameter. At frequencies $\omega < \omega_0$, the magnetic response is essentially static, while at $\omega > \omega_0$, it is suppressed by the skin effect, and at $\omega = \omega_0$ it has a dissipation maximum.

The normalized response of an individual grain can then be expressed by a Debye susceptibility of the form

$$\chi(\omega) = \frac{1}{1 + {\rm j}\omega/\omega_0}\,. \tag{29}$$

At the $\omega = \omega_0$, $-{\rm Im}(\chi)$ has its maximum, while ${\rm Re}(\chi)$ crosses over from 1 to 0 as ω increases. To generalize this simple model to a medium composed of many grains of different sizes, subject to some nonzero DC bias, we proceed as follows. For a given grain with diameter a_0, we replace ω_0 in (29) by a bias dependent frequency $\omega_{\rm cro}(I_{\rm DC})$, defined as in (28) but with bias dependent incremental permeability

$\mu_{\mathrm{ri}}(I_{\mathrm{DC}})$. $\omega_{\mathrm{cro}}(I_{\mathrm{DC}})$ increases with increasing I_{DC} since $\mu_{\mathrm{ri}}(I_{\mathrm{DC}})$ decreases. Moreover, the effective zero-frequency permeability $\mu_{\mathrm{r}}(0, I_{\mathrm{DC}})$ must be monotonic as a function of $\mu_{\mathrm{ri}}(I_{\mathrm{DC}})$ and thus also decrease. We may therefore posit an (approximate) relation of the form

$$\omega_{\mathrm{cro}}(I_{\mathrm{DC}}) \approx \omega_0 \left[\frac{\mu_{\mathrm{r}}(0, I_{\mathrm{DC}})}{\mu_{\mathrm{r}}(0,0)} \right]^{-\beta} , \tag{30}$$

with some exponent $\beta > 0$ to be determined from measurements. Furthermore, we assume that the volume fraction of different grain sizes in the powder material is described by a log-normal distribution with its maximum at a_0; in other words, the diameters of individual grains are of the form $\mathrm{e}^t a_0$, where t is normal-distributed with mean 0 and some variance $\lambda > 0$. This assumption is in reasonable agreement with observations [41]. Since ω_{cro} is proportional to a_0^{-2}, we can then express the frequency- and bias-dependent relative permeability $\mu_{\mathrm{r}}(\mathrm{j}\omega, I_{\mathrm{DC}})$ in the following form:

$$\mu_{\mathrm{r}}(\mathrm{j}\omega, I_{\mathrm{DC}}) \approx \mu_{\mathrm{r}}(0, I_{\mathrm{DC}}) F_\lambda \left(\frac{\mathrm{j}\omega}{\omega_{\mathrm{cro}}(I_{\mathrm{DC}})} \right) , \tag{31}$$

were F_λ is a dimensionless scaling function defined as

$$F_\lambda(x) = \frac{1}{\sqrt{2\pi\lambda}} \int_{-\infty}^{\infty} \frac{\mathrm{e}^{-t^2/2\lambda}}{1 + \mathrm{e}^{2t} x} \mathrm{d}t , \tag{32}$$

In our fitting procedure for the phenomenological model, we have extracted values of the static bias-dependent permeability $\mu_{\mathrm{r}}(0, I_{\mathrm{DC}})$ directly from the low-frequency behavior of our measurement data, so they are considered as experimental input. Consequently, there are only three remaining model parameters for fitting the model to the frequency dependent measurement result, namely, the zero-bias crossover frequency $\omega_0 = 2\pi f_0$, the variance λ of the log-normal grain size distribution, and the bias scaling exponent β. In practice, the integral that defines the scaling function F_λ in (32) is replaced by a sum over a finite number N of discrete values of t, symmetrically placed around zero and with appropriate gaussian weights. This leads to a representation of $\mu_{\mathrm{r}}(\mathrm{j}\omega, I_{\mathrm{DC}})$ with N poles (all located on the negative real axis in the complex $\mathrm{j}\omega$ plane), which also determines the model order of an equivalent circuit representation. A number $N = 9$ of poles turned out to be sufficient for the present purposes, larger N did not improve the accuracy of the fits. Note, however, that we do *not* use the positions and residues of these poles as independent fitting parameters; instead, they are determined by the chosen value of λ and do not increase the number of independent model parameters.

IV. Modeling Results

This section presents the results obtained by using the measured data permeability spectra as input to the macromodeling approaches outlined in the previous sections.

A. Fitting of Permeability Spectra

The permeability spectra determined by measurements were used to derive macromodels for the considered magnetic materials. Table II summarizes the settings used for the black-box modeling and the phenomenological modeling, respectively. The computational effort for generating the black-box macromodels is rather low: for the various materials listed in Table I, the computations took only 16 s, 11 s, 12 s and 15 s, respectively, on an ordinary consumer laptop.

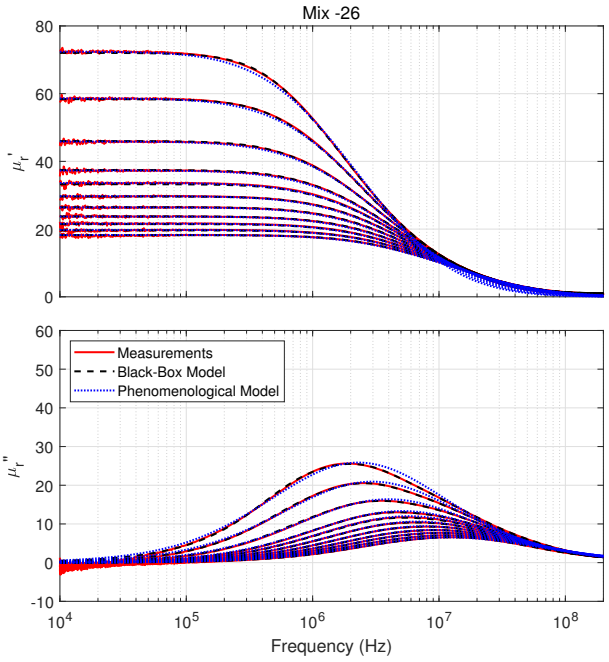

Fig. 4. Measured and fitted complex permeability spectra of material *Mix -26*. The curves correspond to DC bias H-fields $H_{\mathrm{DC}} = n \times (15.7\,\mathrm{Oe})$ with $n = 0, 1, ..., 10$, where the uppermost curve in the low frequency range refers to 0 Oe and the lowermost curve refers to 157 Oe.

TABLE II

Fitting Parameter	Black-Box Model n	Black-Box Model $\bar{\ell}$	Phenomenological Model f_0 (MHz)	Phenomenological Model λ	Phenomenological Model β
Mix -26	9	4	2.3	0.34	1.2
Mega Flux	5	3	26	0.50	1.5
Kool Mμ MAX	8	4	10	0.80	1.0
MPP	8	4	14.1	0.90	0.5

Figure 4 shows the permeability spectrum of the *Mix -26* material, both as obtained by measurements and as modeled by the outlined approaches. The measured permeability spectra show a typical relaxation behavior with a real part that is decreasing over frequency and a corresponding local maximum of the imaginary part. Furthermore, as the superimposed bias H-field increases, the real permeability decreases and the dissipation peak get shifted to higher frequencies. The black-box model captures those features and exhibits a very good agreement for the entire range of frequencies and bias fields. The phenomenological model also shows a very good agreement with measurements. However, small deviations are noticeable, related to the low number of adjustable parameters of this model (see Sec. III).

The next material investigated is *Mega Flux*. Figure 5 shows its permeability spectrum, again as obtained by measurements and as modeled by the outlined approaches. Again,

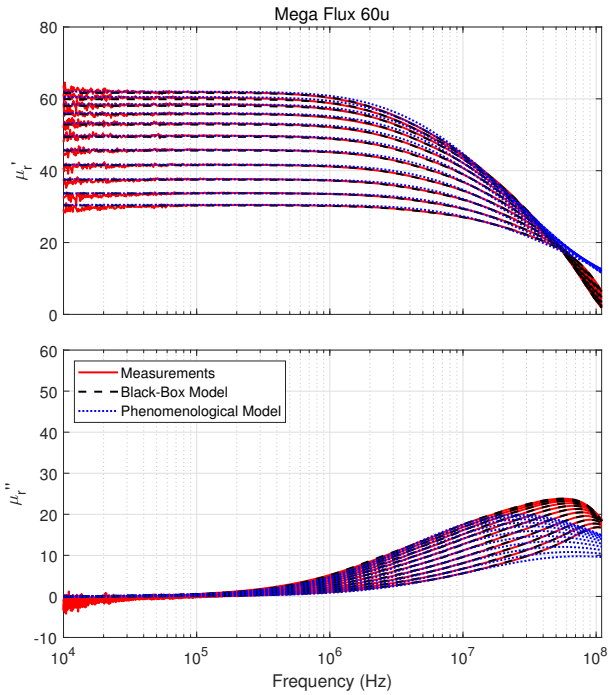

Fig. 5. Measured and fitted complex permeability spectra of material *Mega Flux*. The curves correspond to DC bias H-fields $H_{\mathrm{DC}} = n \times (15.7\,\mathrm{Oe})$ with $n = 0, 1, ..., 10$, where the uppermost curve in the low frequency range refers to 0 Oe and the lowermost curve refers to 157 Oe.

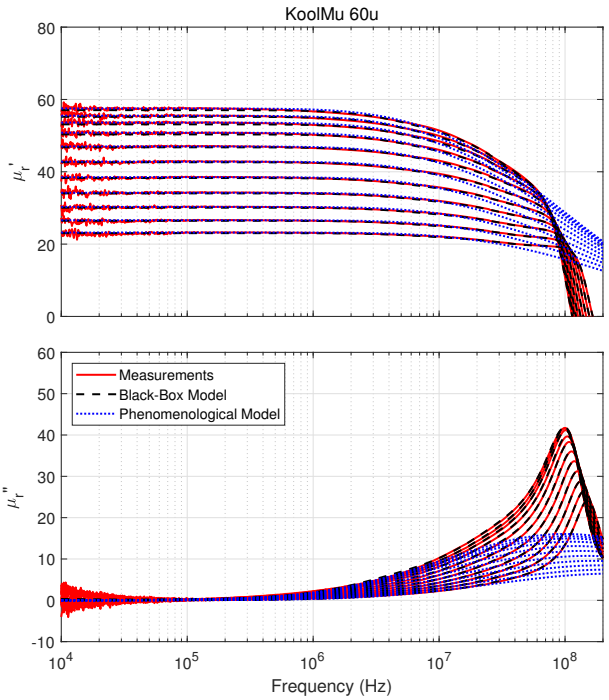

Fig. 6. Measured and fitted complex permeability spectra of material *Kool Mμ MAX*. The curves correspond to DC bias H-fields $H_{\mathrm{DC}} = n \times (15.7\,\mathrm{Oe})$ with $n = 0, 1, ..., 10$, where the uppermost curve in the low frequency range refers to 0 Oe and the lowermost curve refers to 157 Oe.

the black-box model agrees very well with the measurements, whereas the phenomenological model now exhibits significant deviations in the high frequency range, since it is designed to describe only the intrinsic effective permeability of the material. The HF characteristics of *Mega Flux* are governed by two physical effects: 1) a relaxation behavior, due to eddy currents in the individual grains of the powder material (the intrinsic material property), and 2) dimensional resonances depending on the individual size and geometry of the measured core, which were not visible in *Mix -26* (Figure 4) but become relevant in *Mega Flux* due to its higher relative permittivity [22]. As the phenomenological model is tailored to capture the first effect only, deviations occur for this material. It is possible to extend the model to include dimensional resonance effects, albeit at the expense of increased complexity and adding two more fitting parameters. The extended phenomenological model does, however, not attain the level of accuracy of the black-box model, and so we will not discuss it in further detail here.

Figures 6 and 7 show the complex permeability spectra of *Kool Mμ MAX* and *MPP*, respectively. These cores exhibit strong dimensional resonances, in particular their real part turns negative at some tens of MHz. The dimensional resonances are more pronounced than for *Mega Flux*, as the permeability starts to decrease only at higher frequencies. Accordingly, resonances can form at lower frequencies. For these two test cases, the accuracy of the black-box model is in full agreement with that of the previous two examples. Again, a very good agreement up to 10 MHz is observed, whereas the dimensional resonance above is, by construction of the model, not captured.

Please note that the described permeability spectra refer to effective permeabilities associated with certain core dimensions. At high frequencies, those spectra differ from the bulk material permeabilities, as dimensional resonances appear, which we believe are the main cause for the deviation of the simple phenomenological model from the measurements at frequencies above 10 MHz, seen in figures 5, 6, and 7. To minimize deterioration by dimensional resonances, smaller cores can be used for testing [22]. However, the available test setup [15] was designed for rather large cores to handle high bias currents and small cores cannot be tested.

B. Remarks on the application of the black-box approach

When applying the PSK algorithm outlined in Sec. III, the hyper-parameters n and $\bar{\ell}$ must be set by the user. For the application of interest, a simple brute force approach that performs a grid search over an admissible range of hyper-parameters is a viable approach, as the computational effort required to generate a single model is small. This was the strategy applied in this work to determine the most suitable model orders for each test case. In practical scenarios, the maximum allowed value for $\bar{\ell}$ is limited by the number M of available frequency responses, so that in general the relation $2(\bar{\ell}+1) < M$ should hold to avoid overfitting.

Clearly, the availability of a large number of measurements is beneficial for the application of the black box macromodeling algorithm, and how to properly select the sampling points to maximize accuracy is still an open problem (see e.g. [42]). When the macromodel depends only on one free parameter,

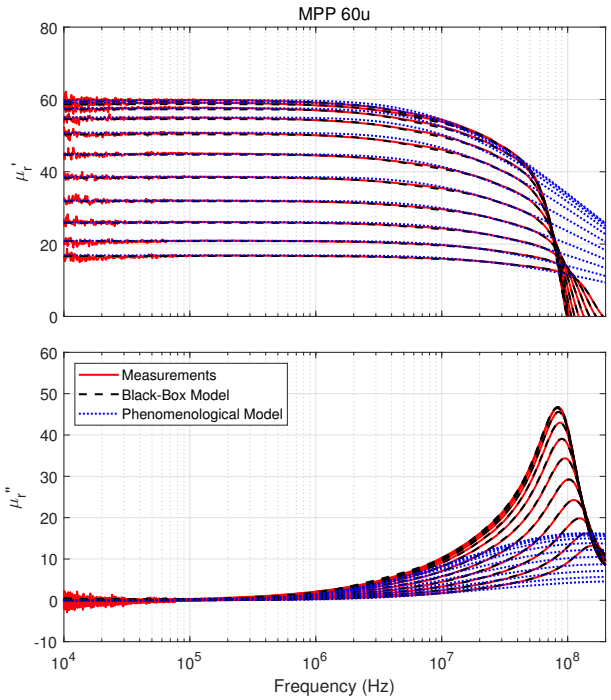

Fig. 7. Measured and fitted complex permeability spectra of material *MPP*. The curves correspond to DC bias H-fields $H_{\mathrm{DC}} = n \times (15.7\,\mathrm{Oe})$ with $n = 0, 1, ..., 10$, where the uppermost curve in the low frequency range refers to 0 Oe and the lowermost curve refers to 157 Oe.

sampling such parameter via uniform gridding is in general an effective choice. Additionally, we point out that, similarly to any black-box, data-driven modeling algorithm, the approach presented here is intended to generate models that are reliable only within the bandwidth where measurements are available. Hence, the modeling bandwidth should be carefully chosen in advance to meet the specifications of the final model operating conditions.

A final remark on convergence is in order. Since the employed PSK algorithm can be interpreted as a parameterized version of the VF scheme, convergence cannot be guaranteed in case the data are affected by noise (see [43]). However, the lack of a theoretical convergence proof does not compromise the effectiveness of the approach — the VF iteration cannot be proved to converge in general either, although VF is the de facto standard approach for rational approximation.

C. Time-Domain Validation

To validate the correct SPICE implementation of the macro-models, we have conducted time-domain anlyses of a simple LC resonant circuit, shown in Fig. 8. A single-turn inductor made of one *Mix -26* toroidal core (dimensions see Tab. I.) and an ideal capacitor with 1 μF are connected in series. The circuit is excited by a 1 V pulse with 50 ns rise time. The inductor is biased by a DC current I_{Bias} ($= I_{\mathrm{DC}}$).

Figure 9 shows the response current to the rising edge of the voltage pulse for four different values of I_{Bias}. Results have been obtained using the black-box model and the phenomenological model, respectively. In general a very good agreement between the two models is observed, validating

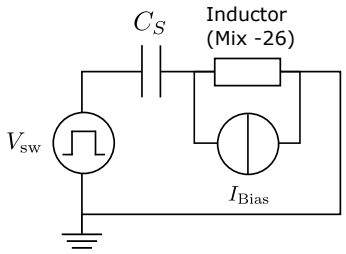

Fig. 8. Resonant circuit with a single core *Mix -26* inductor (properties are listed in I) for time-domain comparison of black-box model and phenomenological model. The resonant circuit is excited by a voltage pulse.

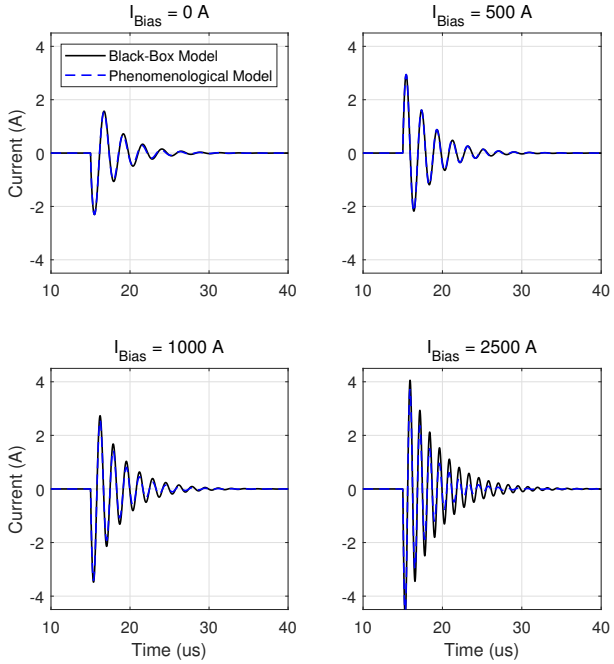

Fig. 9. Response current to raising edge of a voltage pulse exciting the resonant circuit depicted in Fig. 8.

the correct SPICE implementation of both. A slightly higher resonance frequency and higher damping is observed for the phenomenological model, as the real part of the permeability is slightly lower and the imaginary part is slightly higher than in the black-box model. It is worth noting that the frequency content of each of the signals shown in Fig. 8 is confined to some band around the individual resonance frequency, which in turn lies in the range of about 0.2–0.4 MHz, so this step response behavior is not expected to be sensitive to details of the spectrum shown in Figure 4 at higher frequencies (say, above about 1 MHz).

D. Accuracy Analysis

To quantify the accuracy of both modeling approaches, we have evaluated the root mean square (RMS) value of the relative difference between measured data a_n^{meas} and a_n^{mod} for all N data points (all frequencies and all bias currents) according to:

$$\epsilon_{\mathrm{RMS}} = \sqrt{\frac{1}{N}\sum_{n=1}^{N}\left|\frac{a_n^{\mathrm{meas}} - a_n^{\mathrm{mod}}}{a_n^{\mathrm{meas}}}\right|^2}. \qquad (33)$$

Table III summarizes the RMS errors for both macromodels and all four considered materials. Furthermore, the table lists the number of circuit elements required by each approach.

The phenomenological model exhibits an error of less than 5 % for the *Mix -26* material, while the error is larger than 10 % for *Mega Flux* and *Kool MμMAX*, reflecting the inability of the phenomenological model to represent the dimensional resonances occuring between 70 MHz and 100 MHz. In the phenomenological model, the number of circuit elements is the same for all materials, determined by the chosen number of terms in the sum approximating the integral in (32). In contrast, the number of circuit elements of each black-box equivalent circuit depends on the employed model order n. For the considered test cases, the number of circuit elements ranges from 45 to 77. These larger equivalent circuits allow for a substantially higher accuracy than the simple phenomenological approach: for all of the considered materials, the black-box approach commits a relative RMS error below 1.5 % against the reference data.

E. Discussion on available alternative methods

Other modeling approaches for high-frequency magnetic properties under DC bias are based on Foster-type lumped circuits with LR elements [20]. Circuit element values are fitted to measurements using a nonlinear least-squares method [44] and machine learning [21], respectively. Although good results have been demonstrated for certain materials, the applicability of those models is limited, as a fixed circuit topology is assumed (i.e., a LR Foster circuit with predefined number of elements). Effects such as dimensional resonances cannot be modeled and accordingly the technique is not appropriate for ferrites nor powder core materials that are the main focus of this paper.

Regarding fully black-box machine learning techniques, Neural Networks (NN) have been extensively applied for the approximation of parameterized frequency responses in the last decade . When dealing with passive components, approaches are available (e.g., [45]) to guarantee that the predicted frequency responses fulfill the required passivity requirements, while they give up on preserving the rational representation of the reduced order model. Therefore, this kind of methods do not allow for a straight conversion of the model into an equivalent circuit format. Following a different philosophy, the so called Neuro-transfer function approaches [46] build surrogates in the form of rational functions with parameterized coefficients, hence exploiting a model structure which is analogue to (9). Although in principle this kind of models admit a lumped equivalent circuit representation and proved to be effective when dealing with a large number of design parameters, they are mostly used to perform frequency domain analyses, as the corresponding equivalent circuit can not be guaranteed passive over the desired parameter space, but only locally [47]. See also the discussion in [46, Sec.V] and references therein about this topic.

In summary, to the best of the authors knowledge, the proposed black-box modeling approach is the only viable strategy to build accurate parameterized passive equivalent circuits with the aim of performing transient system-level simulations.

TABLE III

	Black-Box Model		**Phenomenological Model**	
	RMS Error	# Circuit Elements	RMS Error	# Circuit Elements
Mix -26	1.38 %	77	4.90 %	10
Mega Flux	1.05 %	45	10.50 %	10
Kool MμMAX	1.29 %	69	12.33 %	10
MPP	1.08 %	69	20.5 %	10

V. Application Examples

Examples for the application of the described macromodels are outlined in the following. We have considered the generic converter setup illustrated in Fig. 10. The high frequency behavior of the converter is described by a multi-port RLGC network which is excited by a noise voltage V_{sw}. The high frequency current path extends via high-frequency impedances Z_{HF} between each end of the converter and ground. A low-frequency current I_{LF} is assumed to flow through the converter. Two EMI filters can be placed in the (both high- and low-frequency) current path, as illustrated. Accordingly, the EMI filter is exposed to the (high) LF current.

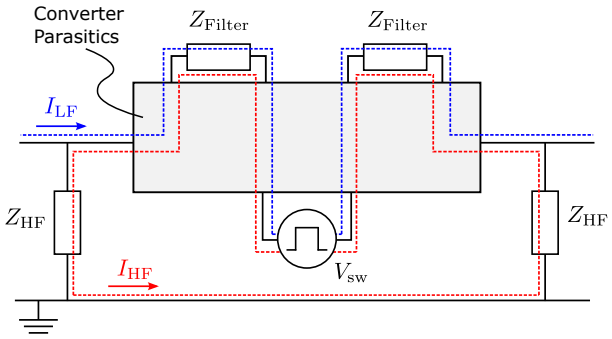

Fig. 10. Equivalent circuit of generic converter setup including parasitic elements of the converter, two EMI filters, high frequency terminations at each end, and a excitation voltage source.

A. System Response Analysis

The first example is to study the high-frequency response I_{HF} of the converter when excited by a broadband voltage of 1 V. For this study, the converter was terminated with a series RC circuit (50 Ω and 10 nF) at each end. Furthermore, we have considered an exemplary EMI filter consisting of a single-turn inductor including *Kool MμMAX* cores. Figure 11 shows the computed system response of the converter up to 10 MHz with and without EMI filters. If no filters are used, pronounced resonances above 4 MHz occur, where the highest amplitude appears around 6 MHz. By introducing EMI filters, those resonances are attenuated. Considering the 6 MHz resonance, the attenuation for this example is around 20 dB in case of 0 Oe bias, whereas it is around 10 dB in case of 150 Oe bias. As the superimposed bias current on the EMI filter significantly influences the electromagnetic noise, it is

important to have macromodels for the permeability spectra under DC bias.

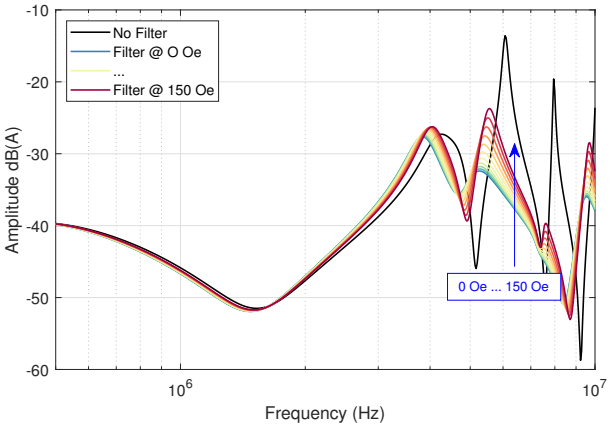

Fig. 11. High frequency current I_{HF} of the converter as response to a 1 V broadband excitation. Black line: Without EMI filter, colored lines: with EMI filter and superimposed DC current. Bias currents are indicated by the line color, where blue corresponds to 0 Oe and red to 150 Oe.

B. Switching Analysis

The next section illustrates the time-domain current response of the converter described above. Now, the converter is excited by a pulse train with 5 KHz switching frequency, 50 % duty cycle, a pulse amplitude of 1 kV and $4\,\mathrm{kV}/\mu s$ turn-on and turn-off slopes. The current response is shown in Fig. 12: the current is capacitive and the current impulses result mainly from the charging of the stray capacitance at the converter terminals. A significant ringing appears when no EMI filter is considered. Using an EMI filter reduces this ringing effectively. However, a bias current on the EMI filter reduces the ringing attenuation. This effect is well visible in the frequency spectrum of the noise current, where the attenuation is highest for unbiased EMI filters.

C. High-Frequency Inductor Design

Designing high-frequency inductors, e. g., for EMI filters, is typically a multi-objective optimization. For instance, a certain inductance at a certain frequency shall be achieved, while minimizing the losses, the volume, and the cost of the inductor. Finding the best trade-off between the conflicting objectives (inductance, losses, volume, ...) depends on the particular application for which an optimization is carried out. Consider a toroidal magnetic core with fixed inner and outer diameter. The frequency- and bias-dependent inductance of the core is proportional to both its permeability and its volume V, i. e., $L \propto \mu_r(I_{\mathrm{DC}}, \omega)V$.

To estimate the permeability of different materials under DC bias when optimizing an inductor, one can use the permeability spectrum for zero bias multiplied by the saturation behavior under DC-bias α:

$$\mu_{\mathrm{r}}(\mathrm{j}\omega, I_{\mathrm{DC}}) \approx \mu_r(\mathrm{j}\omega, 0) \cdot \alpha(I_{\mathrm{DC}}) \tag{34}$$

Both functions can typically be found in data sheets. However, (34) is not always a good approximation of the HF permeability under DC-bias, which motivated the work described in this paper. To improve on the simple approximation (34), one can use the more accurate models described in this work.

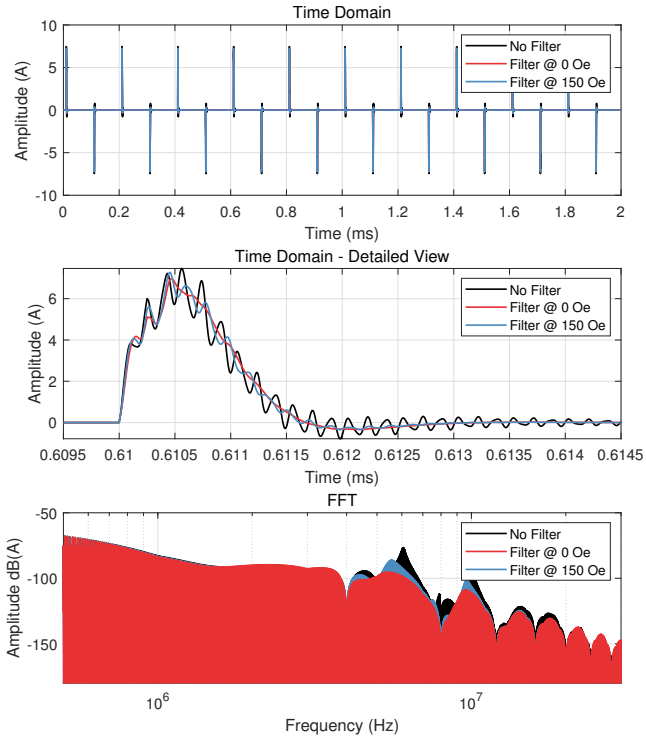

Fig. 12. Illustration of noise current in time-domain (top) and frequency domain (bottom) for the generic converter shown in Fig. 10 when excited by a 5 kHz pulse train. Three different configurations are considered: without EMI filter, with un-biased EMI filter (0 Oe) and with biased EMI filter (150 Oe).

We have considered the following optimization example: an inductor shall be designed for target inductance at 5 MHz based on toroidal cores having fixed inner and outer diameters. The free parameters for this design are the height of the core as well as the magnetic material of the core. Here, we have considered the materials *Mega Flux*, *Kool Mu*, and *MPP* with nominal permeability $\mu_{\mathrm{r}} = 60$ and the high frequency spectra shown in section IV-A. An individual calculation of the core height has been conducted for each material. Figure 13 shows the volume of inductors for different materials as a function of bias H-fields. Results have been obtained by the HF models (black-box models) developed in this work and the simple, data sheet models (34). The results demonstrate the following: at low bias currents, the *Mega Flux* inductor has a higher volume due to a lower permeability at 5 MHz than the other two materials. With increasing bias field, the permeability of the other materials declines faster and hence the volume increases faster than for *Mega Flux*. At the maximum bias field of 150 Oe, the volumes obtained by the simple model and the HF model differ by less than 3 % for *MPP* and more than 12 % for *Mega Flux*. Those differences are due to the fact that *MPP* has a rather flat frequency behavior around 5 MHz (see Fig. 7), while *Mega Flux* exhibits a significant decline (see Fig. 5). Consequently, HF models are required especially for materials which exhibit a significant permeability variation in the frequency range of interest.

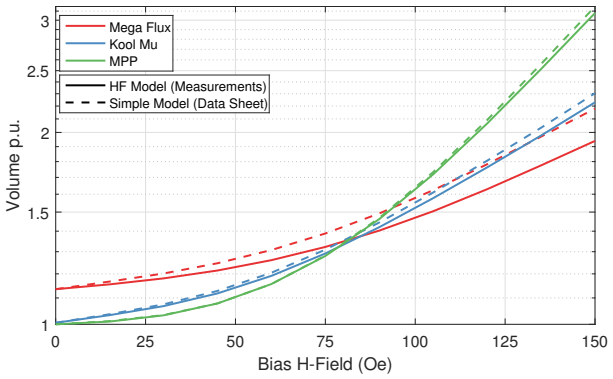

Fig. 13. Volume of inductor at 5 MHz depending on bias H-field for three different materials. Calculations are based on proposed HF models derived from measurements and simple models derived from data sheets, respectively.

VI. Conclusions

This work describes the application of two different parameterized macromodeling approaches, a black-box model and a phenomenological model, for modeling the permeability spectra of magnetic powder materials under DC bias. It is demonstrated that the black-box approach is capable to provide very accurate models for the entire range of frequencies between 10 kHz and 100 MHz. The phenomenological approach in its present, simple form leads to inaccuracies between 10 MHz and 100 MHz when applied to cores that exhibit a dimensional resonance in this range. The resulting SPICE circuits of both approaches have been tested and validated in time and frequency domain circuit simulations. Application examples illustrate the importance of accurate macromodels including the DC bias effect of magnetic materials.

In future work, the phenomenological model should be extended to include dimensional resonance effects. Furthermore, other relevant magnetic materials, such as nanocrystalline materials, should be modeled with the described black-box approach. Here, the temperature dependence of the material could be incorporated as additional parameter of the black-box model.

References

[1] M. S. Rylko, B. J. Lyons, J. G. Hayes, and M. G. Egan, "Revised magnetics performance factors and experimental comparison of high-flux materials for high-current DC–DC inductors," *IEEE Transactions on Power Electronics*, vol. 26, no. 8, pp. 2112–2126, 2011.

[2] M. Kacki, M. S. Rylko, J. G. Hayes, and C. R. Sullivan, "Magnetic material selection for EMI filters," in *2017 IEEE Energy Conversion Congress and Exposition (ECCE)*, 2017, pp. 2350–2356.

[3] Y. Wang, G. Calderon-Lopez, and A. J. Forsyth, "High-frequency gap losses in nanocrystalline cores," *IEEE Transactions on Power Electronics*, vol. 32, no. 6, pp. 4683–4690, 2017.

[4] Y. Liu, H. A. Mantooth, J. Carlos Balda, and C. Farnell, "A variable inductor based LCL filter for large-scale microgrid application," *IEEE Transactions on Power Electronics*, vol. 33, no. 9, pp. 7338–7348, 2018.

[5] J. Imaoka, K. Okamoto, M. Shoyama, Y. Ishikura, M. Noah, and M. Yamamoto, "Modeling, magnetic design, simulation methods, and experimental evaluation of various powder cores used in power converters considering their DC superimposition characteristics," *IEEE Transactions on Power Electronics*, vol. 34, no. 9, pp. 9033–9051, 2019.

[6] H. Shokrollahi and K. Janghorban, "Soft magnetic composite materials (SMCs)," *Journal of Materials Processing Technology*, vol. 189, no. 1, pp. 1–12, 2007.

[7] M. L. Heldwein and J. W. Kolar, "Impact of EMC filters on the power density of modern three-phase PWM converters," *IEEE Transactions on Power Electronics*, vol. 24, no. 6, pp. 1577–1588, 2009.

[8] D. O. Boillat, F. Krismer, and J. W. Kolar, "EMI filter volume minimization of a three-phase, three-level T-type PWM converter system," *IEEE Transactions on Power Electronics*, vol. 32, no. 4, pp. 2473–2480, 2017.

[9] B. Wunsch, S. Skibin, V. Forsstrom, and T. Christen, "Broadband modeling of magnetic components with saturation and hysteresis for circuit simulations of power converters," *IEEE Transactions on Magnetics*, vol. 54, no. 11, pp. 1–5, 2018.

[10] B. Wunsch, S. Skibin, T. Christen, and V. Forsstrom, "Improved EMC filter performance of ferrite cores based on hysteresis and saturation," in *2019 International Symposium on Electromagnetic Compatibility - EMC EUROPE*, 2019, pp. 444–449.

[11] X. Liu, F. Grassi, G. Spadacini, S. A. Pignari, F. Trotti, N. Mora, and W. Hirschi, "Behavioral modeling of complex magnetic permeability with high-order debye model and equivalent circuits," *IEEE Transactions on Electromagnetic Compatibility*, vol. 63, no. 3, pp. 730–738, 2021.

[12] S. Dobák, J. Füzer, P. Kollár, M. Strečková, R. Bureš, and M. Fáberová, "A comprehensive complex permeability approach to soft magnetic bulk cores from pure or resin coated fe and pulverized alloys at elevated temperatures," *Journal of Alloys and Compounds*, vol. 695, pp. 1998–2007, 2017.

[13] D. Smugala, W. Piasecki, M. Ostrogorska, M. Florkowski, M. Fulczyk, and O. Granhaug, "Wind turbine transformers protection method against high-frequency transients," *IEEE Transactions on Power Delivery*, vol. 30, no. 2, pp. 853–860, 2015.

[14] R. Phukan, X. Zhao, C.-W. Chang, D. Dong, R. Burgos, M. Debbou, A. Platt, and P. Asfaux, "Enhanced three-phase ac common-mode filter with optimized damping network for vfds," *IEEE Transactions on Industry Applications*, vol. 59, no. 4, pp. 4274–4286, 2023.

[15] A. Schröder, A. Savca, and D. Bormann, "High frequency permeability measurements and modeling of magnetic powder cores under dc bias," *IEEE Transactions on Power Electronics*, vol. 39, no. 12, pp. 16 361–16 370, 2024.

[16] J. Muhlethaler, J. Biela, J. W. Kolar, and A. Ecklebe, "Core losses under the DC bias condition based on steinmetz parameters," *IEEE Transactions on Power Electronics*, vol. 27, no. 2, pp. 953–963, 2012.

[17] Y. Ishikura, J. Imaoka, M. Noah, and M. Yamamoto, "Core loss evaluation in powder cores: A comparative comparison between electrical and calorimetric methods," in *2018 International Power Electronics Conference (IPEC-Niigata 2018 -ECCE Asia)*, 2018, pp. 1087–1094.

[18] H. Li, D. Serrano, T. Guillod, S. Wang, E. Dogariu, A. Nadler, M. Luo, V. Bansal, N. K. Jha, Y. Chen, C. R. Sullivan, and M. Chen, "How magnet: Machine learning framework for modeling power magnetic material characteristics," *IEEE Transactions on Power Electronics*, vol. 38, no. 12, pp. 15 829–15 853, 2023.

[19] X. Shen, Y. Zuo, J. Kong, and W. Martinez, "Artificial intelligence applications in high-frequency magnetic components design for power electronics systems: An overview," *IEEE Transactions on Power Electronics*, vol. 39, no. 7, pp. 8478–8496, 2024.

[20] M. Szewczyk, K. Kutorasinski, J. Pawłowski, W. Piasecki, and M. Florkowski, "Advanced modeling of magnetic cores for damping of high-frequency power system transients," *IEEE Transactions on Power Delivery*, vol. 31, no. 5, pp. 2431–2439, 2016.

[21] P. Leszczynski, K. Kutorasinski, M. Szewczyk, and J. Pawłowski, "Machine-learned models for power magnetic material characteristics," *IEEE Transactions on Power Electronics*, pp. 1–9, 2024.

[22] A. Schröder, A. Savca, and T. Christen, "Dimensional resonances in magnetic powder cores," in *2024 International Symposium on Electromagnetic Compatibility – EMC Europe*, 2024, pp. 517–522.

[23] S. Grivet-Talocia and B. Gustavsen, *Passive Macromodeling: Theory and Applications*. London, New York: John Wiley & Sons, 2015.

[24] S. Grivet-Talocia, "On driving non-passive macromodels to instability," *International Journal of Circuit Theory and Applications*, vol. 37, no. 8, pp. 863–886, 2009. [Online]. Available: https://onlinelibrary.wiley.com/doi/abs/10.1002/cta.499

[25] D. Deschrijver, T. Dhaene, and D. De Zutter, "Robust parametric macromodeling using multivariate orthonormal vector fitting," *IEEE Transactions on Microwave Theory and Techniques*, vol. 56, no. 7, pp. 1661–1667, 2008.

[26] T. Bradde, P. Toledo, M. De Stefano, A. Zanco, S. Grivet-Talocia, and P. Crovetti, "Enabling fast power integrity transient analysis through parameterized small-signal macromodels," in *2019 International Symposium on Electromagnetic Compatibility - EMC EUROPE*, 2019, pp. 759–764.

[27] A. C. Rodriguez, L. Balicki, and S. Gugercin, "The p-aaa algorithm for data-driven modeling of parametric dynamical systems," *SIAM Journal on Scientific Computing*, vol. 45, no. 3, pp. A1332–A1358, 2023. [Online]. Available: https://doi.org/10.1137/20M1322698

[28] A. Zanco, S. Grivet-Talocia, T. Bradde, and M. De Stefano, "Uniformly stable parameterized macromodeling through positive definite basis functions," *IEEE Transactions on Components, Packaging and Manufacturing Technology*, vol. 10, no. 11, pp. 1782–1794, 2020.

[29] T. Bradde, S. Grivet-Talocia, A. Zanco, and G. C. Calafiore, "Data-driven extraction of uniformly stable and passive parameterized macromodels," *IEEE Access*, vol. 10, pp. 15 786–15 804, 2022.

[30] B. D. Anderson and S. Vongpanitlerd, *Network analysis and synthesis: a modern systems theory approach*. Dover Publications, 2013.

[31] S. Grivet-Talocia and R. Trinchero, "Behavioral, parameterized, and broadband modeling of wired interconnects with internal discontinuities," *IEEE Transactions on Electromagnetic Compatibility*, vol. 60, no. 1, pp. 77–85, 2018.

[32] D. Deschrijver, T. Dhaene, and D. De Zutter, "Robust parametric macromodeling using multivariate orthonormal vector fitting," *IEEE Transactions on Microwave Theory and Techniques*, vol. 56, no. 7, pp. 1661–1667, 2008.

[33] T. Bradde, S. Grivet-Talocia, P. Toledo, A. V. Proskurnikov, A. Zanco, G. C. Calafiore, and P. Crovetti, "Fast simulation of analog circuit blocks under nonstationary operating conditions," *IEEE Transactions on Components, Packaging and Manufacturing Technology*, vol. 11, no. 9, pp. 1355–1368, 2021.

[34] A. Carlucci, T. Bradde, S. Grivet-Talocia, S. Mongrain, S. Kulasekaran, and K. Radhakrishnan, "A compressed multivariate macromodeling framework for fast transient verification of system-level power delivery networks," *IEEE Transactions on Components, Packaging and Manufacturing Technology*, vol. 13, no. 10, pp. 1553–1566, 2023.

[35] P. Triverio, S. Grivet-Talocia, and M. S. Nakhla, "A parameterized macromodeling strategy with uniform stability test," *IEEE Transactions on Advanced Packaging*, vol. 32, no. 1, pp. 205–215, 2009.

[36] B. Gustavsen and A. Semlyen, "Rational approximation of frequency domain responses by vector fitting," *IEEE Transactions on Power Delivery*, vol. 14, no. 3, pp. 1052–1061, 1999.

[37] T. Bradde, S. Grivet-Talocia, M. De Stefano, and A. Zanco, "A scalable reduced-order modeling algorithm for the construction of parameterized interconnect macromodels from scattering responses," in *proc. IEEE Symp. Electromag. Compat. Signal Integrity Power Integrity*. Long Beach, CA, USA: IEEE, 2018, pp. 650–655.

[38] B. Gustavsen, "Improving the pole relocating properties of vector fitting," *IEEE Transactions on Power Delivery*, vol. 21, no. 3, pp. 1587–1592, 2006.

[39] S. Boyd and L. Vandenberghe, *Convex optimization*. Cambridge university press, 2004.

[40] T. Bradde *et al.*, "Parameterized macromodeling of passive and active dynamical systems," 2022.

[41] Z. Guo, J. Wang, W. C. D. Chen, H. Sun, Z. Xue, and C. Wang, "Crystal-like microstructural finemet/fesi compound powder core with excellent soft magnetic properties and its loss separation analysis," *Materials and Design*, vol. 192, p. 10876, 2020.

[42] E. Fevola, A. Zanco, S. Grivet-Talocia, T. Bradde, and M. De Stefano, "An adaptive sampling process for automated multivariate macromodeling based on hamiltonian-based passivity metrics," *IEEE Transactions on Components, Packaging and Manufacturing Technology*, vol. 9, no. 9, pp. 1698–1711, 2019.

[43] S. Lefteriu and A. C. Antoulas, "On the convergence of the vector-fitting algorithm," *IEEE Transactions on Microwave Theory and Techniques*, vol. 61, no. 4, pp. 1435–1443, 2013.

[44] K. Kutorasinski, J. Pawlowski, P. Leszczynski, and M. Szewczyk, "Nonlinear modeling of magnetic materials for circuit simulations," *Scientific Reports*, vol. 13, no. 1, oct 2023. [Online]. Available: https://doi.org/10.1038/s41598-023-44187-3

[45] H. M. Torun, A. C. Durgun, K. Aygün, and M. Swaminathan, "Causal and passive parameterization of s-parameters using neural networks," *IEEE Transactions on Microwave Theory and Techniques*, vol. 68, no. 10, pp. 4290–4304, 2020.

[46] P. Zhang, F. Feng, W. Liu, J. Chen, K. Ma, and Q.-J. Zhang, "Systematic neuro-transfer function parametric modeling with a compact embedded format," *IEEE Transactions on Microwave Theory and Techniques*, pp. 1–17, 2024.

[47] Z. Guo, J. Gao, Y. Cao, and Q.-j. Zhang, "Passivity enforcement for passive component modeling subject to variations of geometrical parameters using neural networks," in *2012 IEEE/MTT-S International Microwave Symposium Digest*, 2012, pp. 1–3.

Arne Schröder (M'16) received the Diploma degree and the Ph.D. degree in electrical engineering from the Hamburg University of Technology, Hamburg, Germany, in 2009 and 2014, respectively. From 2014 to 2017, he was a postdoctoral researcher at the Institute of Applied Physics, University of Bern, Bern, Switzerland. He joined ABB Corporate Research in 2017 and since 2020, he is with Hitachi Energy Research, Baden-Dättwil, Switzerland. His research interests include electromagnetic design and analysis of power electronic equipment as well as modeling of complex and multiscale systems. Dr. Schröder received the IEEE TRANSACTIONS ON ELECTROMAGNETIC COMPATIBILITY Best Paper Award in 2015.

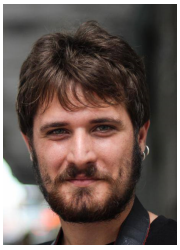

Tommaso Bradde received the B.Sc. degree in electronic engineering from Rome Tre University, Rome, Italy, in 2015, and the M.Sc. degree in mechatronic engineering and the Ph.D. degree in electrical, electronic and communications engineering from the Politecnico di Torino, Turin, Italy, in 2018 and 2022, respectively. He is currently a Researcher and an Assistant Professor with the Politecnico di Torino. His current research interests include data-driven parameterized macromodeling and its applications to system-level signal and power integrity assessments, with the inclusion of active devices. Dr. Bradde was a co-recipient of the 2018 Best Paper Award of the IEEE International Symposium on Electromagnetic Compatibility, the 2020 and 2022 Best Paper Awards of the IEEE Conference on Electrical Performance of Electronic Packaging and Systems, and the Best Student Paper Award of the 23rd IEEE Workshop on Signal and Power Integrity.

Dierk Bormann received the Ph.D. degree in physics from the University of Heidelberg, Germany, in 1992. After some years of academic research in the fields of statistical physics, superconductivity, and low-dimensional quantum systems, he joined in 2000 ABB Corporate Research, Västerås, Sweden, where his worked focused mainly on transient and HF modeling of power apparatus and systems. He also supervised research students at the Royal Institute of Technology (KTH) in Stockholm, and at Mälardalens University (MDU) in Västerås. Since 2020 he is with Hitachi Energy Research in Västerås. His current research interests include the stability analysis and control of power electronic converters, transient dynamics and EMC in converter stations, as well as the mathematical modeling of electromagnetic and thermal material properties.

Alexandru Savca received the M.Sc. degree in Power Electronics from the University of Twente, Enschede, the Netherlands, in 2024. His academic focus included battery technology, electromagnetic design and analysis, and thermal modelling of power electronic equipment. In 2025 he joined Hitachi Energy in the BiMOS Backend division in Lenzburg, Switzerland.

Stefano Grivet-Talocia (M'98–SM'07–F'18) received the Laurea and Ph.D. degrees in electronic engineering from the Politecnico di Torino, Turin, Italy in 1994 and 1998, respectively. From 1994 to 1996, he was with the NASA/Goddard Space Flight Center, Greenbelt, MD, USA. He is currently a Full Professor of electrical engineering with the Politecnico di Torino. He co-founded the academic spinoff company IdemWorks (Turin, Italy) in 2007, serving as the President until its acquisition by CST in 2016. He has authored about 250 journal and conference papers. His current research interests include passive macromodeling of lumped and distributed interconnect structures, model-order reduction, modeling and simulation of fields, circuits, and their interaction, wavelets, time-frequency transforms, and their applications. Dr. Grivet-Talocia was a co-recipient of the 2007 Best Paper Award of the IEEE TRANSACTIONS ON ADVANCED PACKAGING. He received the IBM Shared University Research Award in 2007, 2008, and 2009 and an Intel Strategic Research Segment Grant in 2022, 2023 and 2024. He was an Associate Editor of the IEEE TRANSACTIONS ON ELECTROMAGNETIC COMPATIBILITY from 1999 to 2001 and He is currently serving as Associate Editor for the IEEE TRANSACTIONS ON COMPONENTS, PACKAGING AND MANUFACTURING TECHNOLOGY. He was the General Chair of the 20th and 21st IEEE Workshops on Signal and Power Integrity (SPI2016 and SPI2017), the co-Chair of SPI2023 and the Program co-Chair of SPI2024.